



**HAL**  
open science

## Time-resolved laser-induced fluorescence spectroscopy and chemometrics for fast identification of U(VI)-bearing minerals in a mining context

Jean-Baptiste Sirven, Stephanie Szenknect, Evelyne Vors, Eddie Anzalone,  
Sofian Benarib, Papa-Masserigne Sarr, Pascal Reiller, Adel Mesbah, Nicolas  
Dacheux, Thomas Vercoouter, et al.

### ► To cite this version:

Jean-Baptiste Sirven, Stephanie Szenknect, Evelyne Vors, Eddie Anzalone, Sofian Benarib, et al..  
Time-resolved laser-induced fluorescence spectroscopy and chemometrics for fast identification of  
U(VI)-bearing minerals in a mining context. *Spectrochimica Acta Part A: Molecular and Biomolecular  
Spectroscopy* [1994-...], 2023, 296, pp.122671. 10.1016/j.saa.2023.122671 . cea-04187821

**HAL Id: cea-04187821**

**<https://cea.hal.science/cea-04187821>**

Submitted on 25 Aug 2023

**HAL** is a multi-disciplinary open access archive for the deposit and dissemination of scientific research documents, whether they are published or not. The documents may come from teaching and research institutions in France or abroad, or from public or private research centers.

L'archive ouverte pluridisciplinaire **HAL**, est destinée au dépôt et à la diffusion de documents scientifiques de niveau recherche, publiés ou non, émanant des établissements d'enseignement et de recherche français ou étrangers, des laboratoires publics ou privés.

1 **Time-resolved laser-induced fluorescence spectroscopy and chemometrics for**  
2 **fast identification of U(VI)-bearing minerals in a mining context**

3 *Jean-Baptiste Sirven<sup>a,\*</sup>, Stéphanie Szenknect<sup>b</sup>, Evelyne Vors<sup>a</sup>, Eddie Anzalone<sup>b</sup>, Sofian*  
4 *Benarib<sup>b</sup>, Papa-Masserigne Sarr<sup>a</sup>, Pascal E. Reiller<sup>a</sup>, Adel Mesbah<sup>c</sup>, Nicolas Dacheux<sup>b</sup>, Thomas*  
5 *Vercouter<sup>a,1</sup>, Michaël Descostes<sup>d,e</sup>*

6 <sup>a</sup> Université Paris-Saclay, CEA, Service d'Etudes Analytiques et de Réactivité des Surfaces  
7 (SEARS), F-91191 Gif-sur-Yvette, France.

8 <sup>b</sup> ICSM, Univ Montpellier, CEA, CNRS, ENSCM, Site de Marcoule, Bagnols-sur-Cèze, France.

9 <sup>c</sup> IRCELYON, CNRS – UCBL, 2 avenue Albert Einstein, 69626 Villeurbanne Cedex, France.

10 <sup>d</sup> ORANO Mining, Environmental R&D Dpt., 125 avenue de Paris, 92320 Chatillon, France.

11 <sup>e</sup> Centre de Géosciences, MINES Paris, PSL Research University, Paris, France.

12

13 <sup>1</sup> present address: Université Paris-Saclay, CEA, Service d'Etudes des Matériaux Irradiés  
14 (SEMI), F-91191 Gif-sur-Yvette, France

15

16 \* Corresponding author: [jean-baptiste.sirven@cea.fr](mailto:jean-baptiste.sirven@cea.fr)

17

18

19 **Abstract**

20 We evaluated the potential of time-resolved laser-induced fluorescence spectroscopy (TRLFS)  
21 combined with chemometric methods for fast identification of U(VI)-bearing minerals in a  
22 mining context. We analyzed a sample set which was representative of several environmental  
23 conditions. The set consisted of 80 uranium-bearing samples related to mining operations,  
24 including natural minerals, minerals with uranium sorbed on the surface, and synthetic phases  
25 prepared and characterized specifically for this study. The TRLF spectra were processed using  
26 the Ward algorithm and the K-nearest neighbors (KNN) method to reveal similarities between  
27 samples and to rapidly identify the uranium-bearing phase and the associated mineralogical  
28 family. The predictive models were validated on an independent dataset, and then applied to  
29 test samples mostly taken from U mill tailings. Identification results were found to be in  
30 accordance with the available characterization data from X-ray diffraction (XRD) and scanning  
31 electron microscopy-energy dispersive X-ray spectrometry (SEM-EDX). This work shows that  
32 TRLFS can be an effective decision-making tool for environmental investigations or geological  
33 prospection, considering the large diversity of uranium-bearing mineral phases and their low  
34 concentration in environmental samples.

35

36 **Keywords**

37 TRLFS; chemometrics; uranium; speciation; environment; identification

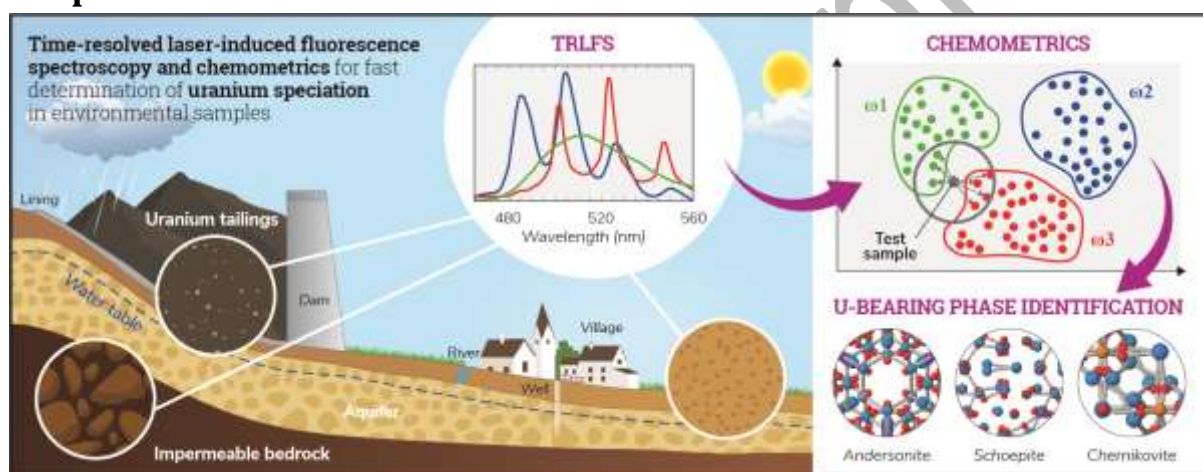
38

39 **Highlights**

- 40
- 41 • A set of 80 natural and synthetic uranium-bearing samples is analyzed by TRLFS
  - 42 • A KNN model is built to identify the mineralogical family and the sample
  - 43 • Predictions of samples from mining sites are consistent with characterization data
  - 44 • Enables fast characterization of uranium-bearing phases in environmental samples
  - 45 • TRLFS has a strong potential as a decision-making tool for environmental studies

45

46 **Graphical Abstract**



47

48

## 49 **1. Introduction**

50 Uranium is a trace element on Earth with a mobility strongly constrained by its chemical  
51 properties and water-rock interactions. In reducing conditions, uranium occurs mostly in its  
52 +IV redox state and is known to precipitate mainly in the form of poorly soluble minerals, such  
53 as uraninite (UO<sub>2</sub>) and/or coffinite (USiO<sub>4</sub>), which are the sources of many deposits [1]-[5]. In  
54 oxidizing conditions, uranium in its +VI redox state is considered to be more mobile. It can  
55 precipitate in neutral to alkaline conditions (e.g. schoepite, meta-schoepite), and in the  
56 presence of inorganic ligands (e.g. phosphate, vanadate, carbonate, sulfate, silicate). It can  
57 also be immobilized by retention processes on the surface of natural minerals (clays, metallic  
58 oxides) and organic matter – see references [6]-[11]. To date, more than 250 U-bearing  
59 minerals have been described in the literature [12]. The coexistence of several uranium phases  
60 within real samples, sometimes at the micrometer scale, is often observed [12]. The mineral  
61 assemblage provides information on the evolution of the in situ physico-chemical conditions.  
62 It is therefore of prime importance to identify the different U-bearing minerals in order to  
63 better understand uranium's mobility, so that appropriate measures to limit their  
64 environmental impact can be taken. This is particularly true in the case of studies on the  
65 formation of uranium deposits, but it is also relevant in order to assess and predict the  
66 environmental footprint of mining sites through the long-term stability of waste rocks and mill  
67 tailings [13]-[16].

68 Several techniques were used to identify the uranium-bearing minerals in natural samples,  
69 these being X-ray diffraction (XRD), scanning electron microscopy – energy dispersive X-ray  
70 spectrometry (SEM-EDX), X-ray absorption spectroscopy (XAS), X-ray photoelectron  
71 spectroscopy (XPS), near-infrared spectroscopy and Raman spectroscopy [17]-[20]. These  
72 techniques can be combined with elemental analysis and/or imaging in order to characterize  
73 uranium minerals and uranium-sorbed phases, but their identification can sometimes be  
74 ambiguous. Although useful, these methods require careful sample preparation and take a  
75 long time to localize traces of uranium in the samples. Consequently, systematic analyses are  
76 very difficult to carry out, and interpretations are usually based on the collection of a few  
77 indications of the presence of uranium-bearing solids. This is the main motivation for  
78 developing an innovative method that would allow faster and systematic detection of uranium  
79 in samples, as well as an identification of the nature of the solids.

80 The luminescence of uranium minerals, which includes both fluorescence and  
81 phosphorescence, has been thoroughly studied since the 1870's [21] [22]. Several emission  
82 bands have been reported above 20 000 cm<sup>-1</sup>. It is well established that the fluorescence of  
83 uranyl originates from its low-lying excited state, and transitions involve molecular orbitals of  
84 the uranyl moiety [23]. The positions of the different emission bands, the spacing between  
85 the bands and their intensities mainly result from the coupling of the electronic transitions  
86 with the vibronic modes of uranyl, i.e. stretching and bending vibrations. Consequently, the  
87 luminescence features are closely related to the coordination chemistry of uranyl in the  
88 compounds, which makes luminescence spectroscopy a very good tool for speciation analysis

89 [24]-[27]. Although luminescence includes both fluorescence and phosphorescence  
90 phenomena, fluorescence is a more widely employed term in the field of spectroscopy and for  
91 that reason it was selected for this study.

92 Time-resolved laser-induced fluorescence spectroscopy (TRLFS) has been particularly used for  
93 the detection and characterization of uranium(VI) compounds taking advantage of its very  
94 high sensitivity and selectivity towards U(VI) [24]-[28], and of the possibility to easily measure  
95 liquid, solid and powdered samples. In TRLFS, a species of interest can be selectively excited  
96 using a laser pulse, in order to measure its fluorescence lifetime, or its fluorescence emission  
97 integrated within a given temporal window after the laser pulse. It is rapid, non-invasive, and  
98 non-destructive, which makes it suitable for investigating natural samples in conjunction with  
99 different techniques. TRLFS has been applied to both synthetic and natural solid compounds.  
100 Many uranium minerals have been characterized by TRLFS, including phosphates, vanadates,  
101 oxides and oxy-hydroxides, carbonates, sulfates, silicates, molybdates, and selenates. In an  
102 early work, deNeufville et al. studied absorption and fluorescence spectra of the uranyl ion in  
103 a collection of rocks, minerals and soils, and measured the fluorescence lifetime [29]. Geipel  
104 et al. characterized about 120 uranium minerals with the aim of building a spectral data bank,  
105 and reported the fluorescence features for a number of phosphates and arsenates [26].  
106 Amayri et al. continued these characterizations on other minerals like becquerelite and  
107 schwartzite [30], as well as phases from the liebigite family [31] [32]. Among the applications  
108 of the technique, Morris et al. investigated uranium-contaminated soils from a former  
109 uranium-processing site in the USA using several spectroscopic techniques like X-ray  
110 absorption spectroscopy, Raman spectroscopy, and TRLFS [33]. Fluorescence spectra were  
111 obtained and compared with those from autunite- and schoepite-like minerals from different  
112 collections. Following a similar methodology, uranium precipitates such as meta-autunite,  
113 phosphuranylite, and uranium(VI) hydroxides were identified in sediments from  
114 contaminated USA sites by combining experimental techniques, including micro-fluorescence  
115 analysis with a 5  $\mu\text{m}$  spot size [34]. Wang et al. also characterized several uranium silicates for  
116 comparison with U(VI)-contaminated sediments in the Hanford site (USA) [35]. As the  
117 fluorescence of some U(VI) compounds may be too low or insufficiently resolved to allow a  
118 correct detection and identification, detection with a higher spectral resolution and a  
119 reduction of the fluorescence quenching effect was achieved using cryogenic TRLFS at Liquid  
120 He Temperature (LHeT) [27]. Although such analyses required a more sophisticated  
121 experimental apparatus, using low-temperature measurements was helpful for identifying  
122 these uranium-bearing phases. TRLFS has been also successfully employed to detect and  
123 characterize uranium(VI) sorbed on mineral phases. Using prepared samples of U(VI) sorbed  
124 on minerals taken as references, Wang et al. concluded that quartz and phyllosilicates were  
125 the main sorbents in sediments responsible for U(VI) uptake [36]. Othmane et al.  
126 characterized uranium-bearing opal from the Nopal deposit in Mexico by TRLFS and other  
127 techniques [37]. They compared the luminescence features with reference uranium samples,  
128 and concluded that uranium may be adsorbed on the mineral as phosphates or polynuclear

129 hydroxide phases. More recently, Mei et al. used TRLFS to study sorption of U(VI) on illite at  
130 different concentrations of dissolved inorganic carbon and variable pH [38].

131 Thus, the effectiveness of TRLFS for detecting uranyl fluorescence even at trace level has  
132 already been shown. However, the assignment of recorded spectra to specific mineral phases  
133 and uranyl-bearing compounds is still challenging. Similarities in the emission features  
134 between mineralogical families and between the phases within a mineralogical family make it  
135 a hard task to unambiguously identify a specific compound. A visual comparison of  
136 experimental spectra to a reference database is rather limited in speed and accuracy [39],  
137 whereas multivariate methods for spectra processing can be very helpful in order to improve  
138 both detection and assignment. These methods have been proven to be efficient in several  
139 applications of laser-induced fluorescence, particularly in biomedical [40] and environmental  
140 [41] fields, and in food science [42]. A few papers have addressed the characterization of  
141 uranium(VI) compounds. Wang et al. were able to draw some of their conclusions using  
142 multivariate curve resolution-alternating least squares (MCR-ALS) to resolve the time-  
143 dependent profiles and the pure spectral components of their samples [36]. The authors  
144 found that TRLF spectra of U(VI) adsorbed on quartz-chlorite mixtures could be matched by a  
145 linear combination of three pure species spectra. Drobot et al. used parallel factor analysis  
146 (PARAFAC) to process 3D data, namely time-resolved spectra at different pH values of uranyl  
147 solutions. Their approach aimed to extract not only the stability constants of mononuclear  
148 uranyl(VI) hydrolysis species, but also the individual emission spectra and fluorescence decays  
149 [43]. Yet, those different studies on uranium(VI) were limited to the analysis of a few uranium-  
150 bearing phases and uranyl complexes in solution. In a natural environment, many different  
151 minerals associated with uranium can be expected. It is therefore relevant to explore how  
152 TRLFS, combined with multivariate methods, can deal with this variability and can be used to  
153 identify a larger range of compounds.

154

155 In this study, a set of TRLF spectra was obtained from 80 uranium-bearing samples  
156 representative of environmental contexts [44] and especially related to uranium mining  
157 operations, including natural minerals, minerals with uranium sorbed on the surface, and  
158 synthetic phases. Initially, Ward clustering was first performed to reveal similarities between  
159 the samples. Then, a predictive K-nearest neighbors (KNN) model was built to identify the  
160 uranium-bearing phase and the associated mineralogical family. The models were validated  
161 on an independent dataset, and then applied to the TRLF spectra of other samples, particularly  
162 those from mining sites. The obtained identification performances demonstrate the feasibility  
163 of fast and sensitive speciation analysis of environmental uranium compounds.

164

165

166 **2. Materials and methods**

167 **2.1. Samples**

168 80 samples were assembled for this study. They are listed in Table 1, with the dominant  
169 uranium phase previously determined by different characterization techniques when  
170 available. About 58% (46 samples) were synthetic samples prepared specifically in order to  
171 have well-controlled reference samples for the chemometric identification model. These  
172 samples were in powder form. Clay samples were prepared using adsorption of uranyl on the  
173 surface of clay minerals, with a concentration ranging from 10 to 900 ppm, except for the MX  
174 003 sample which had 3834 ppm of uranium. Other uranium phases were prepared by specific  
175 synthesis protocols. The samples were characterized by X-ray Diffraction (XRD),  
176 Thermogravimetric Analysis (TGA), Raman and Infrared Spectrometry, and Scanning Electron  
177 Microscopy (SEM). Details of the synthesis and characterization of most synthetic training  
178 samples are given in the Supplementary Materials, as well as for two samples from the  
179 validation set.

180 The remaining samples were natural, either taken from the Orano Mining mineralogical  
181 collection (17 samples), or sourced from three U mill tailings storage facilities located in France  
182 (17 samples): Bellezane (Haute-Vienne), Cellier (Lozère), and Ribière (Creuse). Those samples  
183 were in the form of small solid fragments. The samples from the mineralogical collection had  
184 previously been characterized by XRD and SEM. A few of them were not homogeneous, with  
185 the presence of two dominant uranium phases, sometimes not clearly identified. They were  
186 subsequently treated as distinct samples, labelled A and B. As for the mining sites samples,  
187 some of them were characterized independently with the techniques cited above.

188

189  
190  
191

Table 1 Samples used in this study. The training, validation, and test sets refer to the chemometric model. MC: mineralogical collection. For the Torbernite samples the brackets refer to the sampling site. Question marks mean that the dominant mineralogical family and/or the main uranium phase were not clearly identified by characterization techniques.

	Sample name	Synthetic / natural	Dominant mineralogical family	Main uranium phase	Reference
Training set	Acetate	synt	Other	$\text{UO}_2(\text{CH}_3\text{COO})_2 \cdot 2\text{H}_2\text{O}$	ICSM21-01
	Andersonite	synt	Carbonates	$\text{Na}_2\text{Ca}(\text{UO}_2)(\text{CO}_3)_3 \cdot 6\text{H}_2\text{O}$	LANIE15-01
	Ankoleite	synt	Phosphates	$\text{K}_2(\text{UO}_2)_2(\text{PO}_4)_2 \cdot 6\text{H}_2\text{O}$	ICSM15-01
	Autunite	nat	Phosphates	$\text{Ca}(\text{UO}_2)_2(\text{PO}_4)_2 \cdot 10\text{-}12\text{H}_2\text{O}$	(MC)
	Autunite (synthetic)	synt	Phosphates	$\text{Ca}(\text{UO}_2)_2(\text{PO}_4)_2 \cdot 10\text{-}12\text{H}_2\text{O}$	ICSM15-02
	Becquerelite 055	synt	Oxy-hydroxides	$\text{Ca}(\text{UO}_2)_6\text{O}_4(\text{OH})_6 \cdot n\text{H}_2\text{O}$	EA21-055
	Billietite 049	synt	Oxy-hydroxides	$\text{Ba}(\text{UO}_2)_6\text{O}_4(\text{OH})_6 \cdot n\text{H}_2\text{O}$	EA21-049
	Ca and U silicate	synt	Silicates	$\text{Ca}(\text{UO}_2)_2(\text{Si}_2\text{O}_5)_3 \cdot 10 \text{H}_2\text{O}$	SBb-020
	Carnotite	synt	Vanadates	$\text{K}_2(\text{UO}_2)_2(\text{VO}_4)_2 \cdot 3 \text{H}_2\text{O}$	ICSM15-03
	Chernikovite	synt	Phosphates	$(\text{H}_3\text{O})_2(\text{UO}_2)_2(\text{PO}_4)_2 \cdot 6 \text{H}_2\text{O}$	ICSM15-04
	Compreignacite 050	synt	Oxy-hydroxides	$\text{K}_2(\text{UO}_2)_6\text{O}_4(\text{OH})_6 \cdot 8\text{H}_2\text{O}$	EA21-050
	Francevillite	nat	Vanadates	$\text{Ba}(\text{UO}_2)_2(\text{VO}_4)_2 \cdot 5\text{H}_2\text{O}$	(MC)
	Illite 005	synt	Clays	U sorbed on Na-illite	EA21-005
	Kaolinite 008	synt	Clays	U sorbed on Na-kaolinite	EA21-008
	Kaolinite 029	synt	Clays	U sorbed on Na-kaolinite	EA21-029
	Liebigite	synt	Carbonates	$\text{Ca}_2(\text{UO}_2)(\text{CO}_3)_3 \cdot 11 \text{H}_2\text{O}$	LANIE15-02
	Metaschoepite	synt	Oxides	$\text{UO}_3 \cdot 2\text{H}_2\text{O}$	EA20-008
	Metazeunerite	nat	Arsenates	$\text{Cu}(\text{UO}_2)_2(\text{AsO}_4)_2 \cdot 8 \text{H}_2\text{O}$	(MC)
	Na Zippeite	synt	Sulfates	$\text{Na}_5(\text{UO}_2)_8(\text{SO}_4)_4\text{O}_5(\text{OH})_3 \cdot 12\text{H}_2\text{O}$	SBb-015
	Nitrate	synt	Other	$\text{UO}_2(\text{NO}_3) \cdot 6\text{H}_2\text{O}$	ICSM21-02
	Paraschoepite	synt	Oxides	$\text{UO}_3 \cdot 0.8\text{H}_2\text{O}$	EA21-016
	Smectite 035	synt	Clays	U sorbed on Na-smectite	EA21-035
	Smectite 036	synt	Clays	U sorbed on Na-smectite	EA21-036
	Soddyite	synt	Silicates	$(\text{UO}_2)_2\text{SiO}_4 \cdot 2\text{H}_2\text{O}$	SBb-004
	Sulfate	synt	Sulfates	$\text{UO}_2(\text{SO}_4)$	ICSM21-03
	Torbernite (BN42)	nat	Phosphates	$\text{Cu}(\text{UO}_2)_2(\text{PO}_4)_2 \cdot 12\text{H}_2\text{O}$	(MC)
	Torbernite (synthetic)	synt	Phosphates	$(\text{H}_3\text{O})_{0.4}\text{Cu}_{0.8}(\text{UO}_2)_2(\text{PO}_4)_2 \cdot 7.6\text{H}_2\text{O}$	ICSM15-05
	UO3	synt	Oxides	$\text{UO}_3$	ICSM21-04
Uranophane 064	synt	Silicates	$\text{Ca}(\text{UO}_2)_2(\text{SiO}_3\text{OH})_2 \cdot 5\text{H}_2\text{O}$	EA21-064	
Weeksite	synt	Silicates	$\text{K}_2(\text{UO}_2)_2(\text{Si}_5\text{O}_{13}) \cdot 4\text{H}_2\text{O}$	SBb-019	
Zippeite	synt	Sulfates	$\text{K}_3(\text{UO}_2)_4(\text{SO}_4)_2\text{O}_3(\text{OH}) \cdot 3\text{H}_2\text{O}$	SBb-005	
Validation set	Autunite + oxide	nat	Phosphates/Oxides	$\text{Ca}(\text{UO}_2)_2(\text{PO}_4)_2 \cdot 10\text{-}12\text{H}_2\text{O} ?$	(MC)
	Becquerelite 048	synt	Oxy-hydroxides	$\text{Ca}(\text{UO}_2)_6\text{O}_4(\text{OH})_6 \cdot n\text{H}_2\text{O}$	EA21-048
	Boltwoodite	synt	Silicates	$\text{K}(\text{UO}_2)(\text{SiO}_3\text{OH}) \cdot 1.5\text{H}_2\text{O}$	SBb-006
	Illite 004	synt	Clays	U sorbed on Na-illite	EA21-004
	Illite 021	synt	Clays	U sorbed on Na-illite	EA21-021
	Illite 025	synt	Clays	U sorbed on Na-illite	EA21-025
	Kaolinite 007	synt	Clays	U sorbed on Na-kaolinite	EA21-007

	Kaolinite 027	synt	Clays	U sorbed on Na-kaolinite	EA21-027
	Kaolinite 030	synt	Clays	U sorbed on Na-kaolinite	EA21-030
	Kaolinite 032	synt	Clays	U sorbed on Na-kaolinite	EA21-032
	MX 001	synt	Clays	U sorbed on MX80 bentonite	EA21-001
	MX 002	synt	Clays	U sorbed on MX80 bentonite	EA21-002
	MX 018	synt	Clays	U sorbed on MX80 bentonite	EA21-018
	Na and U silicate	synt	Silicates	$\text{Na}_2(\text{UO}_2)_2(\text{Si}_2\text{O}_5)_3 \cdot 10\text{H}_2\text{O}$	SBb-014
	Smectite 010	synt	Clays	U sorbed on Na-smectite	EA21-010
	Smectite 011	synt	Clays	U sorbed on Na-smectite	EA21-011
	Smectite 038	synt	Clays	U sorbed on Na-smectite	EA21-038
	Torbernite (BNL)	nat	Phosphates	$\text{Cu}(\text{UO}_2)_2(\text{PO}_4)_2 \cdot 12\text{H}_2\text{O}$	(MC)
	Torbernite (Margabal)	nat	Phosphates	$\text{Cu}(\text{UO}_2)_2(\text{PO}_4)_2 \cdot 12\text{H}_2\text{O}$	(MC)
	Uranocircite	nat	Phosphates	$\text{Ba}(\text{UO}_2)_2(\text{PO}_4)_2 \cdot 12\text{H}_2\text{O}$	(MC)
Test set	Gummite_A	nat	Silicates / Oxides	$\text{Mg}(\text{UO}_2)_2(\text{SiO}_3\text{OH})_2 \cdot 6\text{H}_2\text{O} + \text{PbO} \cdot \text{UO}_3 \cdot \text{H}_2\text{O}$	(MC)
	Gummite_B	nat	Silicates / Oxides	$\text{Mg}(\text{UO}_2)_2(\text{SiO}_3\text{OH})_2 \cdot 6\text{H}_2\text{O} + \text{PbO} \cdot \text{UO}_3 \cdot \text{H}_2\text{O}$	(MC)
	MX 003	synt	Clays	U sorbed on MX80 bentonite	EA21-003
	Parsonsite	nat	Phosphates	$\text{Pb}_2\text{UO}_2(\text{PO}_4)_2 \cdot 2\text{H}_2\text{O}$	(MC)
	Phosphuranylite	nat	Phosphates	$\text{KCa}(\text{H}_3\text{O})_3(\text{UO}_2)_7(\text{PO}_4)_4\text{O}_4 \cdot 8\text{H}_2\text{O}$	(MC)
	Smectite U1	synt	Clays	U sorbed on smectite	LANIE15-03
	Smectite U4	synt	Clays	U sorbed on smectite	LANIE15-04
	Torbernite (Lachaux A)	nat	Phosphates ?	$\text{Cu}(\text{UO}_2)_2(\text{PO}_4)_2 \cdot 8\text{H}_2\text{O} ?$	(MC)
	Torbernite (Lachaux B)	nat	unknown	?	(MC)
	Unknown_1	nat	Vanadates ?	?	(MC)
	Unknown_2	nat	Silicates or Oxides ?	U sorbed on quartz ?	(MC)
	Unknown_3	nat	Silicates or Oxides ?	U sorbed on quartz ?	(MC)
	Bellezane 11	nat			BZN11
	Bellezane 4	nat			BZN4
	Bellezane 5	nat			BZN5
	Bellezane 6	nat			BZN6
	Bellezane 7	nat			BZN7
	Cellier 1	nat			CE221222T
	Cellier 2	nat			CE230312T
	Cellier 3	nat			CEL11521T
	Cellier 4	nat			CEL161651T
	Cellier 5	nat			CEL21521T
	Cellier 6	nat			CEL232T
	Cellier 7	nat			CEL342T
	Cellier 8	nat			CEL672T
	Ribière 1	nat			Ri0151T
	Ribière 2	nat			Ri1241393T
Ribière 3	nat			Ri1851992TB	
Ribière 4	nat			Ri1992041TBS	

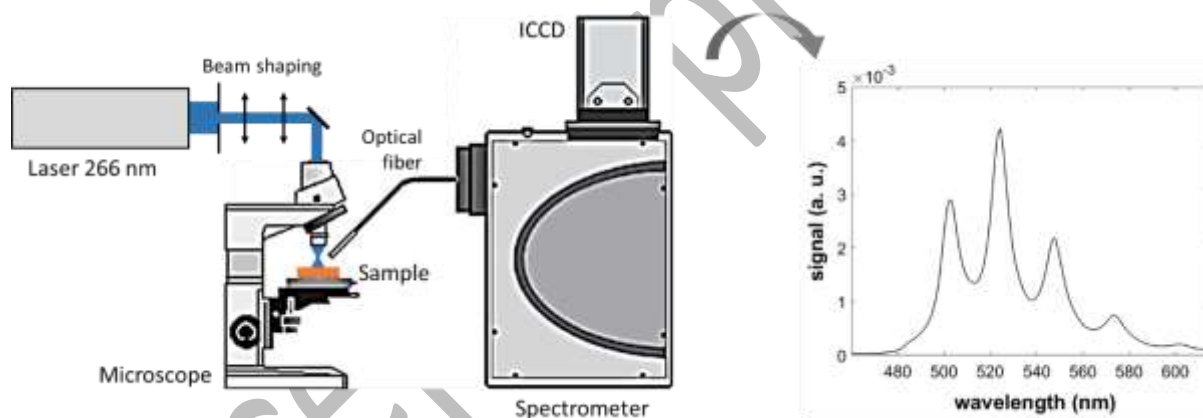
192

193

## 2.2. Experimental apparatus

The experimental apparatus is shown in Figure 1, along with an example of a TRLF spectrum of a uranium-bearing phase. The apparatus included a quadrupled Nd:YAG laser at 266 nm and 10 Hz repetition rate (Minilite I, Continuum). This excitation wavelength is not the most selective, but it is within the uranium(VI) charge-transfer bands and it is a good compromise to induce fluorescence in solid samples of various mineralogical phases. The laser delivered a 5 ns pulse. The laser beam was shaped by a 50- $\mu\text{m}$  aperture linked to an optical system and directed into an Olympus BX51TRF fluorescence microscope equipped with a 15X microscope objective lens (Thorlabs LMU-15X-UVB). The sample surface was placed beyond the focal point so that the sample was illuminated by a 1 mm diameter laser spot without ablating the sample. The pulse energy on the sample was ca. 25  $\mu\text{J}$ . The fluorescence emission was collected using a 1 mm diameter optical fiber positioned at 45° at about 3 mm from the sample surface. It was connected to an SR303i spectrometer (Andor) equipped with a 150  $\mu\text{m}$  slit, a 300 grooves/mm grating and an intensified CCD camera (iStar, Andor) with 2048  $\times$  512 pixels of 13.5  $\mu\text{m}$  cooled to -20°C. The spectrometer was centered at 540 nm and the spectra were recorded between 445 and 635 nm with a linear dispersion of 0.15 nm/pixel.

210



211

212 *Figure 1 Experimental apparatus and example of a TRLF spectrum of a torbernite sample.*

213

214 For the powders, the TRLFS measurements were made on mg-sized samples manually  
215 positioned on an adhesive tape inside a fume hood for safety reasons: to limit the dispersion  
216 of uranium powder and the risk of inhalation. Each spectrum was recorded from 300 laser  
217 shots on the same sample location, with a gate delay of 1  $\mu\text{s}$  after the laser pulse, and an  
218 integration time of 200  $\mu\text{s}$ . For most of the samples, 25 spectra were acquired from different  
219 zones on the sample surface. For some of them, fewer spectra were acquired due to  
220 limitations of the available mass and the sample or powder deposit homogeneity. In total,  
221 about 1 800 spectra were recorded.

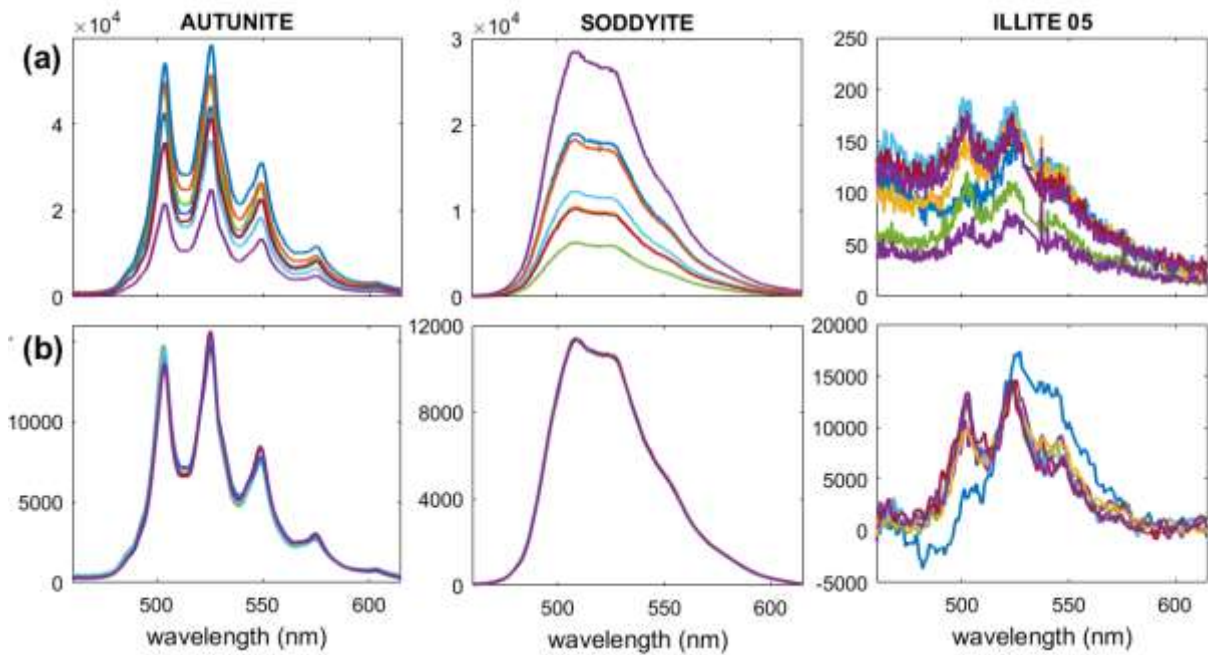
222 Before any data treatment, the electronic background, estimated from the blind zones of the  
223 ICCD, was subtracted from the spectra, and their spectral range was reduced to a span of 460-  
224 615 nm. In addition, the diffusion of the second diffraction order at around 532 nm of the laser  
225 wavelength was sometimes visible. Therefore, the spectral band between 529 and 535 nm  
226 was also removed. In the end, the processed spectra consisted of 1041 pixels. Some spectra  
227 are shown on Figure 2 for autunite, soddyite and illite samples.  
228

### 229 **2.3. Chemometric approach**

230 For chemometric data processing, the samples were allocated to the training, validation, and  
231 test sets (see Table 1). For the training set, we mostly kept synthetic, homogeneous, well  
232 characterized, and sufficiently pure uranium phases that were representative of what could  
233 be found on mining sites. In the particular case of clays, only samples with 300 to 1000 ppm  
234 uranium were included in the training set, because lower concentrations led to a very low  
235 TRLFS signal, while higher concentrations may have induced precipitation issues during the  
236 adsorption process. A few natural samples were particularly homogeneous and showed clean  
237 and intense spectra. Therefore, they were retained as reference samples and were included  
238 in the training set. The same strategy was applied to build the validation set: its samples had  
239 to be well characterized, since this dataset is used to evaluate the model's predictive ability.  
240 The main difference between the training and validation sets lies in the presence of samples  
241 representative of all classes. Whereas all classes are included in the training set, some of them,  
242 for availability reasons, are missing from the validation set, which mainly contains clays – with  
243 a wider uranium concentration range than in the training set – and phosphates. Finally, the  
244 test set contained all the other samples, i.e. three synthetic clay samples, natural samples  
245 from the mineralogical collection whose identification was incomplete or doubtful, and  
246 samples from the mining sites.

247 The spectra from each sample were pre-processed. Firstly, a second-order Savitzky-Golay  
248 smoothing filter over a 31 pixel moving rectangular window [45] was applied. Then, a linear  
249 baseline taken between the minimum and maximum wavelengths was subtracted. Finally, the  
250 spectra were normalized by Multiplicative Signal Correction, a common approach in analytical  
251 spectroscopy [46]. This methodology was optimized through different trials so as to give the  
252 best classification performances. Figure 2 shows the effect of this pre-processing for three  
253 samples: a natural autunite, and two synthetic ones (soddyite SBb-004 and illite 05). It can be  
254 seen that the pre-processing rescales the intensity range of the spectra: the non-processed  
255 spectra of autunite are two orders of magnitude more intense than those of illite 05, while  
256 the pre-processed ones are on the same scale. Another effect is to reduce the variance: it is  
257 clear that pre-processed spectra fluctuate much less than non-processed ones. It is also  
258 helpful in reducing background fluctuations, as observed in the case of illite 05. Finally, it can  
259 reveal the presence of outliers, as shown by the abnormal spectrum visible after pre-  
260 processing the illite 05 spectra.

261



262

263 *Figure 2 (a) non-processed and (b) pre-processed spectra of autunite, soddyite and illite samples. Since the second diffraction*  
264 *order of the laser wavelength was sometimes visible around 532 nm, the spectral band between 529 and 535 nm was removed.*

265

266 The spectral processing was done in two steps. Firstly, an unsupervised analysis was  
267 performed in order to explore the similarities between samples. For that purpose, we used  
268 Ward clustering [47]-[49]. This method enables agglomerative clustering to be performed,  
269 based on the Euclidean distance between the spectra. Clusters are formed such that the intra-  
270 cluster variance is minimized. In a second step, the K-nearest neighbors (KNN) method was  
271 implemented to build a predictive model of the uranium-bearing phase present in the sample.  
272 This supervised algorithm has been shown to be efficient for sample classification in several  
273 papers on fluorescence spectroscopy, see e.g. the recent works [50]-[52]. It also uses the  
274 Euclidean distance between spectra and allocates an unknown spectrum to class  $i$  if samples  
275 of this class are in the majority within its K-nearest neighbors. The value of K was optimized  
276 by a bootstrap method applied to the training set. For each class, the available spectra were  
277 randomly split into a training (70%) and a validation set (30%). A KNN model was calculated  
278 for each value of K between 1 and 10. The model sensitivity and specificity were determined  
279 from the confusion matrix obtained from the validation spectra. Sensitivity is equal to the true  
280 positive rate, whereas specificity is equal to the true negative rate. The average value of these  
281 two indicators over 30 bootstrap iterations enabled us to define the optimum K value, which  
282 was found to be equal to 1.

283 The final predictive model was then calculated for  $K = 1$  based on the whole training set, which  
284 included 31 samples and 886 spectra. Classes were defined in two different ways, either based  
285 on the mineralogical family (see Table 1) (Model 1), or based on the samples, i.e. each sample  
286 was considered as a single class (Model 2). As a result, the training set had 10 and 31 classes,  
287 respectively. Both models were applied to the validation dataset (20 samples, 549 spectra) to

288 discuss the models' predictability on known samples, and finally to the test dataset (32  
289 samples, 443 spectra) to make predictions on (supposedly) unknown or ill-defined samples.

## 290 **3. Results and discussion**

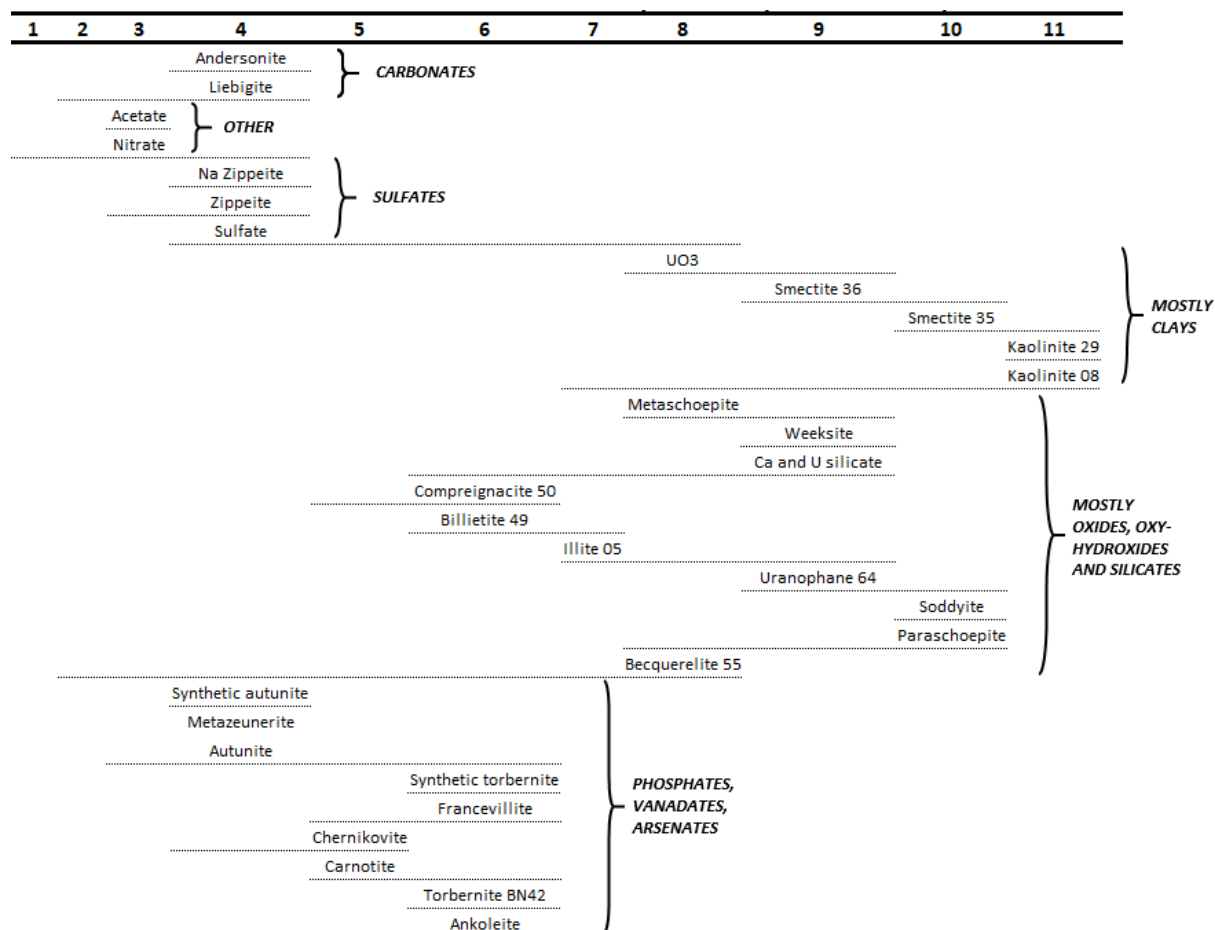
### 291 **3.1. Samples clustering**

292 Figure 3 shows the results of the sample clustering performed on the training set using the  
293 Ward algorithm. The whole set was used to determine a first classification tree. Then, clusters  
294 identified by pruning the tree were used as the inputs for secondary trees. The procedure was  
295 repeated until, ideally, the spectra of all individual samples were isolated in a single tree. The  
296 number of classification trees required to separate each sample is shown in Figure 3. One can  
297 see that this is the case for 29 samples out of 31. Only natural autunite and meta-zeunerite  
298 could not be separated. These two minerals are based upon the same autunite-type sheets of  
299 general formula  $[(\text{UO}_2)(\text{TO}_4)]^-$  (with  $T = \text{P}$  or  $\text{As}$ ). These sheets are made of uranyl square  
300 bipyramids sharing vertices with  $\text{TO}_4$  tetrahedra. Electroneutrality is maintained thanks to  
301 various cations located in the interlayer space between the sheets [53]. Thus, it could be  
302 argued that the coordination polyhedron of  $\text{UO}_2^{2+}$  is equivalent in the two phases, which  
303 would explain the similarity of the TRLF spectra. Surprisingly, the natural autunite spectra are  
304 less similar to those of synthetic autunite, which exhibit the same pattern with fluorescence  
305 bands slightly blue-shifted.

306 One also notes that carbonates from the liebigite family – due to their strong blue-shifted  
307 spectra relative to uranyl [27] [29] [54] –, sulfates, and the group formed by uranyl acetate  
308 and uranyl nitrate, can be isolated in three or four steps. The phosphate, vanadate, and  
309 arsenate samples form a well-defined group, from which each sample can be subsequently  
310 identified in four to six steps, except for natural autunite and meta-zeunerite as previously  
311 mentioned. Four clay samples are found to be close to each other, two smectites and two  
312 kaolinites, while the illite sample seems to be closer to the last group of samples, which  
313 contains the oxides, oxy-hydroxides, and silicates. Nevertheless, each individual sample can  
314 be isolated. The most similar samples require up to 10 to 11 trees for separation to be  
315 achieved.

316 The exploration of the training dataset shows that, as expected, the samples cluster according  
317 to their mineralogical family, or to a consistent group of mineralogical families: it is acceptable  
318 that e.g. phosphates, arsenates, and vanadates are found to be relatively close. The same  
319 applies to e.g. oxides and oxy-hydroxides. This indicates that TRLF spectra measured under  
320 our experimental conditions, and pre-processed as presented above, can be used to build a  
321 predictive model to identify either their mineralogical families, or their uranium-bearing  
322 phases.

323



324

325 *Figure 3 Number of classification trees required to separate spectra of each sample using the Ward algorithm.*

326

### 327 3.2. Identification of uranium-bearing phases

328 We showed in the previous section that unsupervised analysis of TRLF spectra enabled  
 329 samples to be clustered in a consistent way with regard to their mineralogical family. Then, in  
 330 a first step, a KNN predictive model was built, aiming to identify the mineralogical families of  
 331 the training and validation samples (model 1). The second step consisted of building a second  
 332 model to identify the sample, i.e. to obtain a more accurate classification (model 2).

333 The mineralogical family predicted by model 1 on the training set is shown in the  
 334 Supplementary Material. The rate of correct classification is very high in all cases. Only 4 out  
 335 of 886 spectra were not correctly identified. This indicates that the learning process  
 336 encountered no particular problem, and was able to identify all the training samples. Beyond  
 337 that, it is necessary to look at the validation results in order to estimate the model's predictive  
 338 ability. Table 2 shows that three phosphate samples (uranocircite and the two torbernite  
 339 samples) were correctly identified. One can note some confusion (16 %) for one torbernite  
 340 sample with the arsenate phase (meta-zeunerite) represented by a single training sample, for  
 341 which we mentioned in the previous section its similarity with natural autunite, one of the  
 342 samples from the phosphate class. A fourth sample of the mineralogical collection was labeled

343 as a mixture of a phosphate and an oxide phase. The oxide phase was not detected by TRIFS,  
344 so that this sample was attributed mainly to phosphates (80 %), and to a lesser extent to  
345 vanadates (20 %), their spectra being quite similar (see Figure 3). It can be emphasized that  
346 those four samples are natural, the only ones from the validation set, and that the predictions  
347 made by the model are quite consistent with the prior knowledge about them.

348 The validation set included 13 clay samples, including illite, kaolinite, and smectite samples  
349 that are represented in the training set, and three MX80 bentonite samples. The kaolinite  
350 samples were almost perfectly identified, including the kaolinite 032 sample, with the lowest  
351 concentration of adsorbed uranium (11 ppm). The predictions for illite were also very good.  
352 Nevertheless, 15 % of the illite 004 spectra were attributed to the oxy-hydroxide family and  
353 3 % to the oxide family. For the smectites, 76 to 80 % of the spectra were attributed to clays.  
354 The rest were attributed to silicates for two samples. The smectite 038 sample is the least  
355 concentrated in uranium with only 12 ppm. In this case, about a quarter of the spectra were  
356 identified as oxides. The same situation occurred with the bentonite samples, for which the  
357 majority of spectra were identified as clays, while a varying minor fraction (4 to 16 %) was  
358 attributed to silicates or oxides.

359 The last samples of the validation dataset were becquerelite, boltwoodite, and Na and U  
360 silicate ( $\text{Na}_2(\text{UO}_2)_2(\text{Si}_2\text{O}_5)_3 \cdot n\text{H}_2\text{O}$ ). The latter was perfectly identified as a Ca and U silicate  
361 ( $\text{Ca}_2(\text{UO}_2)_2(\text{Si}_2\text{O}_5)_3 \cdot n\text{H}_2\text{O}$ ), clearly the most similar sample of the training set, while the  
362 becquerelite 048 sample was identified as a mixture of oxide and oxy-hydroxide phases. This  
363 is fully consistent with the powder XRD and SEM-EDS characterizations of this synthetic  
364 sample (EA21-048), which revealed that it contained about 61 % becquerelite and 39 %  
365  $\text{UO}_3 \cdot n\text{H}_2\text{O}$ , the latter being used as a synthesis precursor. Finally, boltwoodite was attributed  
366 mainly to clays, with a minority to silicates (18% of spectra). As shown by the powder XRD and  
367 SEM (see Figures S1 and S2 of the Supporting Information), quartz was the main phase in this  
368 sample due to its use in large excess as an Si precursor in the synthesis protocol of  
369 boltwoodite. Thus, the boltwoodite phase was found as a minor one in this sample. Moreover,  
370 the sorption of uranyl on the surface of quartz or silica grains is not fully excluded [37][55][56].  
371 Even if the amount of adsorbed uranyl is assumed to be low, this could explain the confusion  
372 with the clay family for a fraction of the spectra if the probed area was mainly composed of  
373 quartz or silica grains. This could also explain a confusion with the clay family. Another  
374 hypothesis could be that uranyl adsorbed on clays exhibits a similar environment to  
375 boltwoodite, which might explain a possible similarity of the TRIF spectra. Boltwoodite is  
376 based on a layered structure comprising sheets of silica tetrahedra and  $\text{UO}_2^{2+}$  polyhedra  
377 [57][58]. Within these sheets, the almost linear uranyl cation is coordinated to five oxygen  
378 atoms in the equatorial plane, which leads to the formation of ( $\text{UO}_7$ ) pentagonal bipyramids,  
379 one of the most common  $\text{U}^{6+}$  coordinations in solids [59][60]. The  $\text{UO}_7$  bipyramids form edge-  
380 sharing chains connected by ( $\text{SiO}_3\text{OH}$ ) tetrahedra. Three of the vertices of the Si tetrahedron  
381 are occupied by O atoms bonded to one or two  $\text{UO}_2^{2+}$ . The last vertex is occupied by one OH  
382 group weakly bound to a  $\text{K}^+$  cation in the interlayer space. The interlayer also contains water

383 molecules. Kremleva et al. [61] used DFT calculations to simulate uranyl adsorption on two  
 384 common-edge surfaces of smectite clay minerals. They showed that uranyl is adsorbed as  
 385 inner-sphere complexes in a bidentate way on aluminol, silanol or mixed adsorption sites. The  
 386 resulting coordination number of uranium is 7 or 6 at mixed-sites (including the two oxygen  
 387 of the uranyl group). The structural parameters of uranyl surface complexes are determined  
 388 by the nature of these surface sites but are mostly independent of the type of clay minerals.  
 389 Spectroscopic studies also supported this conclusion [18]. This observation could explain the  
 390 confusion between the spectra of uranyl adsorbed on the surface of different clay minerals,  
 391 and potentially with boltwoodite where U-O-Si bonds are also present.

392 Overall, except for the boltwoodite sample, we note that the predictions for the mineralogical  
 393 family of the validation samples were correct for the majority of the spectra, and/or consistent  
 394 with the characterization data. We conclude that this predictive model can be reliably used  
 395 on unknown samples to identify the mineralogical family of uranium-bearing phases.

396

397 *Table 2 Mineralogical family predicted by model 1 on the validation set, expressed as a rate over the total number of spectra*  
 398 *for each sample.*

SAMPLE :	MINERALOGICAL FAMILY :													Becquerelite 048	Autunite + oxide	Torbernite (BNL)	Torbernite (Margabal)	Uranocircite	Boltwoodite	Na and U silicate
	Illite 004	Illite 021	Illite 025	Kaolinite 007	Kaolinite 027	Kaolinite 030	Kaolinite 032	MX 001	MX 002	MX 018	Smectite 010	Smectite 011	Smectite 038							
Reference :																				
Predicted :	Clays													Oxy-hydroxides		Phosphates			Silicates	
Arsenates																0.16				
Carbonates	0.04																			
Clays	0.82	0.96	1.00	0.98	1.00	1.00	0.96	0.84	0.88	0.96	0.80	0.76	0.76			0.82				
Other																				
Oxides	0.03												0.12	0.04		0.24	0.40			
Oxy-hydroxides	0.15																0.56			
Phosphates																0.80	1.00	0.84	1.00	
Silicates				0.02				0.16				0.20	0.24	0.04		0.18	1.00			
Sulfates	0.04																			
Vanadates															0.20					

399

400

401 The same approach was applied to identify the samples (model 2). The Supplementary  
402 Material shows the results for the training set, for which the predictions are perfect for most  
403 of the samples. A few confusions are noticeable, e.g. between becquerelite and  
404 compregnacite. The structure of these two uranium phases is based on sheets of edge-sharing  
405 uranyl pentagonal bipyramids, also called  $\alpha$ -U<sub>3</sub>O<sub>8</sub>-type sheets [53][62]. The interlayer  
406 between these sheets allows the presence of various cations including monovalent K<sup>+</sup> or Na<sup>+</sup>  
407 for compregnacite, and divalent Ca<sup>2+</sup> for becquerelite (or Ba<sup>2+</sup> for billietite). Then, the net  
408 charge of the sheet is balanced by hydroxyl ions. The distribution of hydroxyl ions is similar for  
409 the three uranyl oxide hydrates used in this work. This similarity in the topology of uranyl-  
410 containing sheets of becquerelite, compregnacite, and billietite can explain the confusion  
411 between their TRLF spectra. We also note an acceptable confusion between two kaolinite  
412 samples. Other confusions can be considered as random errors or due to outliers. This is  
413 particularly true for the illite sample due to the low signal-to-noise ratio of its spectra and to  
414 the presence of a visible outlier (see Figure 2). Yet, these confusions remain a minority: only  
415 12 training spectra out of 886 were incorrectly classified.

416 Looking now at the validation set results (Table 3), we can see that the predictions for most of  
417 the samples are relatively dispersed. Confusion between very similar TRLF spectra of samples  
418 within the same mineralogical family, as well as the heterogeneity of the natural samples, may  
419 explain this observation. Thus, the four natural samples of the validation set are uranium  
420 phosphates, and were identified as phosphates, arsenates, and vanadates in variable  
421 proportion. Uranocircite was identified as autunite, which is acceptable since both minerals  
422 belong to the autunite group [62], exhibiting the same uranyl phosphate sheets of general  
423 formula [(UO<sub>2</sub>)(PO<sub>4</sub>)]<sup>-</sup>. The interlayer space contains water molecules and Ba<sup>2+</sup> in uranocircite  
424 instead of Ca<sup>2+</sup> in autunite. In addition, as mentioned previously, the spectra of the  
425 autunite/oxide sample are slightly shifted towards shorter wavelengths compared to the  
426 natural autunite of the training set, and were mostly predicted as torbernite, another mineral  
427 of the autunite group containing Cu<sup>2+</sup>. Similarly, torbernite (BNL) was identified as  
428 chernikovite at 76%, the protonated form of this mineralogical family, and as torbernite at  
429 24%: the spectra of these three samples are very similar to each other. Torbernite (Margabal)  
430 has 52% of its spectra attributed to torbernite and 32% to autunite, which is again an  
431 acceptable confusion relating to the important similarity between both phases.

432 The synthetic kaolinite samples were well identified. The illite samples were also attributed to  
433 kaolinite for 45 to 96% of spectra, while illite was found in a lower proportion. The three  
434 smectite samples were attributed primarily to smectite (60 to 80 %), and to a lower extent to  
435  $\alpha$ -uranophane, Ca[(UO<sub>2</sub>)(SiO<sub>3</sub>OH)]<sub>2</sub>·5(H<sub>2</sub>O), which is based on a layered structure with sheets  
436 of UO<sub>7</sub> pentagonal bipyramids and (SiO<sub>3</sub>OH) tetrahedra. The boltwoodite structure is built  
437 with the same uranophane sheets and a confusion was also observed with uranyl adsorbed  
438 on the surface of clay minerals. The confusion between TRLF spectra could arise from the  
439 similarity in the local environment of uranyl in the uranophane sheets to uranyl adsorbed on  
440 silanol surfaces, but experimental and simulation data which could support this hypothesis

441 are lacking. Finally, the MX80 bentonite samples were identified mostly as kaolinite and  
442 smectite, which is consistent, with a minor proportion of oxides and uranophane. The Na and  
443 U silicate ( $\text{Na}_2(\text{UO}_2)_2(\text{Si}_2\text{O}_5)_3 \cdot n\text{H}_2\text{O}$ ) sample was attributed at 100% to the Ca and U silicate  
444 ( $\text{Ca}_2(\text{UO}_2)_2(\text{Si}_2\text{O}_5)_3 \cdot n\text{H}_2\text{O}$ ), the most similar sample within the training set [58]. The  
445 becquerelite sample was mostly identified as a mixture of becquerelite (48%) and  
446 paraschoepite (40%), which is fully consistent with the observations made for model 1 for this  
447 sample. Finally, the boltwoodite sample was here attributed to smectite at 82% and to  
448 soddyite at 18%, which is also in line with what we mentioned for model 1.

449 In conclusion, the predictions given by model 2 are fully consistent with the available  
450 knowledge on the validation samples. Beyond the identification of the sample mineralogical  
451 family, this model gives a more accurate insight of possible uranium-bearing phases in the  
452 samples. Therefore, the model can be used to make predictions on samples that were used  
453 neither for model training nor validation, particularly samples from former French mining  
454 sites.

455

456

Accepted preprint

457  
458

Table 3 Sample predicted by model 2 on the validation dataset, expressed as a rate over the total number of spectra for each sample. For better readability, training samples that were never predicted have been removed from the table.

Reference : Predicted :	Autunite + oxide	Becquerelite 048	Boltwoodite	Illite 004	Illite 021	Illite 025	Kaolinite 007	Kaolinite 027	Kaolinite 030	Kaolinite 032	MX 001	MX 002	MX 018	Na and U silicate	Smectite 010	Smectite 011	Smectite 038	Torbernite (BNL)	Torbernite (Margabal)	Uranocircite
Autunite	0.07																			0.04
Autunite (synthetic)																			0.32	0.88
Becquerelite 055		0.48																		
Billietite 049				0.15																
Ca and U silicate							0.02							1.00						
Carnotite	0.20																			
Chernikovite																		0.76		0.08
Compreignacite 050		0.08																		
Illite 005				0.36		0.44	0.08													0.16
Kaolinite 008				0.27	0.84	0.52	0.70	0.46	0.64	0.84										
Kaolinite 029				0.18	0.12	0.04	0.12	0.54	0.36	0.08			0.68							
Liebigite										0.04										
Metazeunerite																				0.16
Paraschoepite		0.40		0.03										0.04					0.24	
Smectite 035											0.12		0.32							
Smectite 036			0.82				0.08			0.04	0.72	0.20	0.64		0.80	0.76	0.60			
Soddyite			0.18												0.12					
Torbernite (BN42)	0.73																			0.52
Torbernite (synthetic)																			0.24	
UO3													0.12							
Uranophane 064		0.04									0.16				0.08	0.24				
Zippeite					0.04															

459  
460

### 461 **3.3. Analysis of test samples**

462 Both prediction models were used to make predictions on the test set, which consisted mostly  
463 of natural samples. Only the results of model 2 are given here, since the identification of the  
464 uranium-bearing phase a fortiori enables the identification of the mineralogical family. Table  
465 4 shows the obtained predictions, i.e. the most similar samples of the training set, whose  
466 mineralogical family is also noted in the table. Most of the test samples originate from three  
467 U mill tailings storage facilities located in France: Bellezane (samples BZNxx), Cellier (samples  
468 CExx), and Ribière (samples Rixx). Three synthetic clay samples are also part of the test set.  
469 Finally, nine natural samples were also predicted, among which most of them were also partly  
470 characterized by reference techniques, mainly SEM-EDS and XRD (see Table 1).

471 Regarding the synthetic samples, the two smectites (U1 and U4) and the bentonite (MX 003)  
472 were clearly attributed to smectite, consistent with what we observed for the validation  
473 samples. For the natural samples collected from the Bellezane former mining site,

474 Table 4 shows that two samples were mostly identified as oxides, one as silicate, one as  
475 carbonate, and the last one as clay. Previous characterization of those samples showed that  
476 they contained mostly uraninite, uranium adsorbed on smectite, phosphate, and carbonate  
477 phases associated to traces of calcite [15]. The identification of  $UO_3$  and paraschoepite  
478  $UO_3 \cdot 0.8H_2O$  in samples BZN7 and BZN11 is consistent with a possible oxidation of uraninite.  
479 Sample BZN5 was clearly identified as a carbonate, while sample BZN6 is attributed to  
480 kaolinite. Confusion between smectite and kaolinite was not observed for predictions of the  
481 validation set (Table 3). Yet, the sorption efficiency of uranium is much higher on smectite  
482 compared to kaolinite due to a significantly higher cation exchange capacity, therefore the  
483 presence of smectite is more plausible here. The mineralogical family remains consistent  
484 anyway. Sample BZN4 was attributed mostly to soddyite, a silicate, and to clay minerals to a  
485 lesser extent. Composition similarities between silicates and clays could explain this  
486 identification.

487 Previous characterization of the samples from the Cellier mining site gave the same results as  
488 for the Bellezane ones, except that no carbonates were found at the latter. One can see that  
489 paraschoepite was again identified by model 2 as a primary constituent of two samples  
490 (CE230312T, CEL21521T), with a fraction of clay minerals in the latter. Clays were also  
491 identified in four samples. Three of them were mostly attributed to kaolinite (70 % to 90 % of  
492 spectra) with a lower fraction of smectite and illite (CE221222T, CEL11521T, CEL342T). The  
493 fourth one seems to be more balanced between kaolinite and smectite (CEL232T). Predictions  
494 for the last Cellier sample (CEL161651T) were more scattered. Silicate minerals were identified  
495 in half of the spectra, also compreignacite (30 %), paraschoepite (10 %), and illite (10 %).

496 For the Ribière samples, previous characterizations showed a significant presence of  
497 phosphate phases, with also uraninite and U adsorbed on smectite. Predictions show that two  
498 samples were identified as mainly smectite (Ri0151T, Ri1241393T), with also paraschoepite  
499 in the latter. A third one was found as a balanced mixture between those two phases

500 (Ri1851992TB), while the last one (Ri1992041TBS) is mostly attributed to the silicate  
501 uranophane.

502 In addition to these observations, it is interesting to note that the minerals that control the  
503 retention of uranium in the three different mill tailings are the same. This is consistent with a  
504 similar uranium mineralogy in the ore, namely uraninite and coffinite. This is also in line with  
505 a similar ore treatment with sulfuric acid, leading to oxidative dissolution of the uranium(IV)  
506 phases. Alternatively, adsorption on surfaces (e.g. clays) can happen, particularly if the  
507 solubility limit of schoepite has not been reached.

508 The remaining samples of the test set were all natural, with a variable heterogeneity. Prior  
509 characterization by XRD of the two gummite samples (A and B) showed the presence of  
510 silicates and oxides, most probably  $Mg(UO_2)_2(SiO_3OH)_2 \cdot 6H_2O$  and  $PbO \cdot UO_3 \cdot nH_2O$ ,  
511 respectively. These samples were found to be relatively similar. TRLFS analysis showed that  
512 sample B indeed seems to be a silicate, while sample A appears to be a mixture of clay minerals  
513 (69%), with a phosphate and/or an arsenate phase.

514 Three other natural samples were supposed to be predominantly phosphate phases:  
515 parsonsite, phosphuranylite, and torbernite (Lachaux A). One can see that parsonsite was  
516 mostly attributed to meta-zeunerite, an arsenate phase (43%), with fractions of phosphates  
517 (29% autunite and 14% torbernite) and clay minerals (14%). As shown in section 3.1,  
518 meta-zeunerite and autunite spectra are among the most similar of the training set and  
519 confusion between those two phases is therefore possible. Phosphuranylite was predicted as  
520 an equal mixture of autunite and francevillite. The torbernite sample (Lachaux A) was mostly  
521 attributed to torbernite, but also to francevillite. This is in line with previous analyses of this  
522 sample that revealed the presence of metatorbernite  $Cu(UO_2)_2(PO_4)_2 \cdot 8H_2O$  and of two  
523 unidentified uranium-bearing phases in lower concentrations. The other torbernite sample  
524 (Lachaux B), for which no prior information was available, was associated with clay minerals.

525 The last three unknown samples were mostly identified as clay minerals as well (1 and 3), with  
526 also 50% paraschoepite for sample Unknown\_2. This is consistent with the available data on  
527 those samples, except for sample Unknown\_1 for which several vanadate phases were found  
528 by SEM and XRD. Although the training set included two vanadate minerals (francevillite and  
529 carnotite), such phases were not detected by TRLFS. The possible coexistence of three or four  
530 mineral phases within the same sample might lead to a complex spectrum resulting from this  
531 particular mixture, and making the identification difficult.

532 Overall, as with the validation samples, predictions of the test samples were found reasonably  
533 consistent with previous characterizations obtained by reference techniques. In the case of  
534 the environmental samples addressed here, three limitations can be mentioned. Firstly, laser-  
535 induced fluorescence of uranium compounds is efficient for uranium (VI) but not for uranium  
536 (IV). Secondly, some elements like iron are known to be quenchers of uranium fluorescence  
537 [63]. Iron concentration can be significant in mining and natural sites, which may reduce the

538 detection efficiency. Thirdly, identification performance obviously depends on the  
539 representativity and balance of the training set. The confusion observed between meta-  
540 zeunerite, the only arsenate sample, and autunite, might be resolved if more samples from  
541 this mineralogical family were available. This would enable its variability to be better  
542 represented, and confidence in predictions of arsenates to be improved.

543 Despite these limitations, it is worth noting that chemometric analysis of TRLF spectra is a  
544 relevant tool to rapidly identify the uranium-bearing phase in a sample, or at least its  
545 mineralogical family, with a sensitivity consistent with the expected low concentration of  
546 uranium in environmental samples. It has a strong potential as an identification technique for  
547 speciation analysis of uranium samples, in combination with techniques like SEM-EDS, XRD  
548 and Raman spectroscopy, which enable other physical and chemical properties to be  
549 determined, and have different detection limits. Finally, the possibility of making several  
550 localized measurements on the sample also enables the sample homogeneity to be evaluated.

551

Accepted preprint

552  
553

Table 4 Predictions of model 2 on the test set, expressed as a rate over the total number of spectra for each sample, with the maximum rate shown in bold for each test sample. For better readability, training samples that were never predicted have been removed from the table. The associated mineralogical family is noted in the first column.

Mineralogical family :	Test sample : Predicted sample :	BZN11	BZN4	BZN5	BZN6	BZN7	CE221222T	CE230312T	CEL11521T	CEL161651T	CEL21521T	CEL232T	CEL342T	CEL672T	Gummite_A	Gummite_B	MX-003	Parsonsite	Phosphuranylite	Ri0151T	Ri1241393T	Ri1851992TB	Ri1992041TBS	Smectite U1	Smectite U4	Torbernite (Lachaux A)	Torbernite (Lachaux B)	Unknown_1	Unknown_2	Unknown_3	
		Arsenates	Metazeunerite														0.08		<b>0.43</b>	0.04											
Carbonates	Andersonite			<b>0.5</b>																											
	Liebigite			<b>0.5</b>																											
Clays	Illite 005						0.1			0.1				0.1	0.1	<b>0.23</b>		0.14										0.1	<b>0.54</b>	0.2	
	Kaolinite 008							<b>0.5</b>						<b>0.4</b>	0.3										0.12						
	Kaolinite 029		0.2		<b>1.0</b>		0.4		<b>0.7</b>		0.1	0.4	<b>0.4</b>	<b>0.5</b>	<b>0.23</b>					0.1					0.04		<b>0.6</b>	0.15		0.11	
	Smectite 035		0.1						0.2		0.1	<b>0.5</b>		0.1	0.15		<b>0.96</b>			0.4	<b>0.7</b>	0.1		<b>1.0</b>	0.28	0.1		0.2	<b>0.56</b>		
	Smectite 036										0.1				0.08		0.04			<b>0.5</b>	0.1	<b>0.4</b>	0.1		<b>0.56</b>	0.2	0.31	0.1	0.28		
Oxides	Paraschoepite					<b>1.0</b>		<b>1.0</b>		0.1	<b>0.7</b>										0.2	<b>0.4</b>	0.2							<b>0.5</b>	
	UO3	<b>0.8</b>																													
Oxy-hydroxides	Compreignacite 050	0.2								0.3																					
Phosphates	Autunite												0.1		<b>0.23</b>			0.29	<b>0.48</b>												
	Chernikovite																										0.07				
	Torbernite																		0.14							<b>0.60</b>					
Silicates	Ca and U silicate									<b>0.4</b>						<b>0.92</b>															
	Soddyite		<b>0.7</b>						0.1			0.1																			
	Uranophane 064									0.1												0.1	<b>0.7</b>								0.06
Vanadates	Carnotite															0.08															
	Francevillite																		<b>0.48</b>							0.33					

554

## 555 **4. Conclusion**

556 Improving scientific knowledge about uranium-bearing phases can improve the assessment of  
557 the mobility of uranium. The objective of this study was to evaluate the potential of time-  
558 resolved laser-induced fluorescence spectroscopy (TRLFS) combined with chemometric  
559 methods to rapidly identify uranium-bearing phases in complex samples, particularly  
560 environmental samples with a variable heterogeneity. We analyzed 80 uranium samples, of  
561 which 34 were natural and 46 synthetic, these having been prepared specifically for this study.  
562 About 1800 spectra were recorded, and the samples were split into three independent sets:  
563 training, validation, and test. First, analysis of the training set by the Ward algorithm revealed  
564 that reference samples clustered according to their mineralogical family, or to a consistent  
565 group of mineralogical families. Therefore, in a second step, we used the K-nearest neighbors  
566 (KNN) technique to build predictive models of the mineralogical family and of the uranium-  
567 bearing phase. In both cases, predictions obtained on the validation set were found to be fully  
568 consistent with the available knowledge on the samples, mostly obtained by SEM-EDS and  
569 XRD. Then, the model predicting the uranium-bearing phase was used to analyze the test  
570 samples, mostly taken from former French mining sites. Overall, results were found to be in  
571 accordance with such characterization data that was available. This confirms that TRLFS  
572 enables fast and sensitive characterization of uranium-bearing phases in environmental  
573 samples, with the potential to easily analyze solid or powder samples. Although laser-induced  
574 fluorescence of uranium compounds is limited to uranium(VI) phases, and may be significantly  
575 quenched by the iron present in many sites, it can be a useful decision-making tool for  
576 environmental investigations, or even possibly for geological prospection, in addition to other  
577 reference laboratory techniques which can take longer and be more cumbersome to operate.

578

## 579 **Acknowledgements**

580 The authors thank Joseph Lautru (ICSM) for the SEM and EDS analyses of the synthetic and  
581 natural samples; Margot Lecointe and Thibault Le Cam for their help in the acquisition of the  
582 TRLF spectra and data processing; Leila Claveau for the synthesis, Christelle Latrille for the XRD  
583 analysis, and Jérôme Varlet for the SEM analysis of liebigite family minerals; and Sébastien  
584 Savoye (CEA) for providing clay materials for the project.

585

586 **References**

587

- 588 [1] Langmuir, D., Uranium solution-mineral equilibria at low temperatures with applications  
589 to sedimentary ore deposits. *Geochimica et Cosmochimica Acta*, 1978. 42(6): p. 547-  
590 569,
- 591 [2] Bruneton, P., and Cuney, M., 2 - Geology of uranium deposits, in: *Uranium for Nuclear*  
592 *Power*. Eds: Ian Hore-Lacy, Woodhead Publishing, 2016, p. 11-52.
- 593 [3] Franz J. Dahlkamp, *Uranium Deposits of the World - USA and Latin America*. Springer  
594 Berlin, Heidelberg, 2010.
- 595 [4] Franz J. Dahlkamp, *Uranium Deposits of the World - Asia*. Springer Berlin, Heidelberg,  
596 2009.
- 597 [5] Franz J. Dahlkamp, *Uranium Deposits of the World - Europe*. Springer Berlin, Heidelberg,  
598 2016.
- 599 [6] Murakami, T., et al., Mobility of uranium during weathering. *American Mineralogist*,  
600 1997. 82(9-10): pp. 888-899.
- 601 [7] Lahrouch, F., et al., Uranium retention on iron oxyhydroxides in post mining  
602 environmental conditions. *Chemosphere*, 2021. 264: 128473.
- 603 [8] Lahrouch, F., et al., Uranium speciation control by uranyl sulfate and phosphate in  
604 tailings subject to a Sahelian climate, Cominak, Niger. *Chemosphere*, 2022. 287: 132139.
- 605 [9] Bordelet, G., et al., Chemical reactivity of natural peat towards U and Ra. *Chemosphere*,  
606 2018. 202: p. 651-660.
- 607 [10] Tayal, A., et al., Uranium speciation in weathered granitic waste rock piles: An XAFS  
608 investigation. *RSC Advances*, 2049. 9: p. 11762-11773.
- 609 [11] Cretaz, F., et al., Solubility properties of synthetic and natural meta-torbernite. *Journal*  
610 *of Nuclear Materials*, 2013. 442: p. 195-207.
- 611 [12] Finch, R., Murakami, T., Systematics and paragenesis of uranium minerals, in: *Uranium:*  
612 *Mineralogy, Geochemistry and the Environment*. Eds: P.C. Burns, R. Finch, Berlin,  
613 Boston: De Gruyter, 2018, pp. 91-180.
- 614 [13] Boekhout, F., et al., Uranium migration and retention during weathering of granitic  
615 waste rock piles. *Applied Geochemistry*, 2015. 58: pp. 123-135.
- 616 [14] Déjeant, A., et al., Evolution and Environmental Impact of Uranium Mill Tailings at  
617 COMINAK mine, Niger: a Multi-Scale Approach. *Science Of The Total Environment*, 2016.  
618 545-546: pp. 340-352.
- 619 [15] Ballini, M., et al., A multi-scalar study of the long-term reactivity of uranium mill tailings  
620 from Bellezane site (France). *Journal of Environmental Radioactivity*, 2020. 218: 106223.
- 621 [16] Chautard, C., et al., Geochemical characterization of U mill tailings (Bois Noirs Limouzat,  
622 France) highlighting the U and <sup>226</sup>Ra retention. *Journal of Environmental Radioactivity*,  
623 2020. 218: p. 106251.
- 624 [17] May, C. C., et al., Analytical techniques for speciation analysis of aqueous long-lived  
625 radionuclides in environmental matrices. *Trends in Analytical Chemistry*, 2008. 27(2): p.  
626 160-168.

- 627 [18] Geckeis, H., et al., Mineral–Water Interface Reactions of Actinides. *Chem. Rev.*, 2013.  
628 113: p. 1016–1062.
- 629 [19] Pan, Z., et al., U(VI) sorption on Ca-bentonite at (hyper)alkaline conditions Phosphate-  
630 Induced Immobilization of Uranium in Hanford Sediments. *Environ. Sc. & Technol.*, 2016.  
631 50(24): p. 13486-13494.
- 632 [20] Baron, F., et al., Use of near infrared spectroscopy for the identification of coffinite and  
633 uranothorite. *Journal of Near Infrared Spectroscopy*, 2014. 22 : pp. 149-152.
- 634 [21] Becquerel E., Mémoire sur l'analyse de la lumière émise par les composés d'uranium  
635 phosphorescents. *Annales de Chimie et de Physique, Série 4*, 1872 : p. 539-579.
- 636 [22] Becquerel H., Relations entre l'absorption de la lumière et l'émission de la  
637 phosphorescence dans les composés d'uranium. *Compte Rendu de l'Académie des*  
638 *Sciences de Paris*, 1885(101) : p. 1252-1256.
- 639 [23] Zhang, Z.Y. and R.M. Pitzer, Application of relativistic quantum chemistry to the  
640 electronic energy levels of the uranyl ion. *Journal of Physical Chemistry A*, 1999. 103(34):  
641 p. 6880-6886.
- 642 [24] Moulin, C., Laszak, I., Moulin, V., and Tondre, C., Time-resolved laser-induced  
643 fluorescence as a unique tool for low-level uranium speciation. *Appl. Spectrosc.*, 1998.  
644 52: pp. 528-535.
- 645 [25] Bernhard, G., Geipel, G., Brendler, V., and Nitsche, H., Uranium speciation in waters of  
646 different uranium mining areas. *J Alloy Compd*, 1998. 271: pp. 201-205.
- 647 [26] Geipel, G., et al., Spectroscopic properties of uranium(VI) minerals studied by time-  
648 resolved laser-induced fluorescence spectroscopy (TRLFS). *Radiochimica Acta*, 2000.  
649 88(9-11): p. 757-762.
- 650 [27] Wang, Z., et al., A cryogenic fluorescence spectroscopic study of uranyl carbonate,  
651 phosphate and oxyhydroxide minerals. *Radiochimica Acta*, 2008. 96(9-11): p. 591-598.
- 652 [28] Moulin, C., et al., Uranium Speciation in Solution by Time-Resolved Laser-Induced  
653 Fluorescence. *Analytical Chemistry*, 1995. 67(2): p. 348-353.
- 654 [29] deNeufville J. P., et al., Selective detection of uranium by laser-induced fluorescence: a  
655 potential remote-sensing technique . 1: Optical characteristics of uranyl geologic  
656 targets. *Applied Optics*, 1981(20): p. 1279-1296.
- 657 [30] Amayri, S., et al., Spectroscopic characterization of synthetic becquerelite,  
658  $\text{Ca}[(\text{UO}_2)_6\text{O}_4(\text{OH})_6].8\text{H}_2\text{O}$ , and swartzite,  $\text{CaMg}[\text{UO}_2(\text{CO}_3)_3].12\text{H}_2\text{O}$ . *Canadian*  
659 *Mineralogist*, 2004. 42: p. 953-962.
- 660 [31] Amayri, S., et al., Spectroscopic characterization of the uranium carbonate andersonite  
661  $\text{Na}_2\text{Ca}[\text{UO}_2(\text{CO}_3)_3].6\text{H}_2\text{O}$ . *Environmental Science & Technology*, 2004. 38(22): p. 6032-  
662 6036.
- 663 [32] Amayri, S., et al., Spectroscopic characterization of alkaline earth uranyl carbonates.  
664 *Journal of Solid State Chemistry*, 2005. 178(2): p. 567-577.
- 665 [33] Morris, D.E., et al., Speciation of uranium in Fernald soils by molecular spectroscopic  
666 methods: Characterization of untreated soils. *Environmental Science & Technology*,  
667 1996. 30(7): p. 2322-2331.

- 668 [34] Hunter, D.B. and P.M. Bertsch, In situ examination of uranium contaminated soil  
669 particles by micro-X-ray absorption and micro-fluorescence spectroscopies. *Journal of*  
670 *Radioanalytical and Nuclear Chemistry*, 1998. 234(1-2): p. 237-242.
- 671 [35] Wang, Z.M., et al., Fluorescence spectroscopy of U(VI)-silicates and U(VI)-contaminated  
672 Hanford sediment. *Geochimica et Cosmochimica Acta*, 2005. 69(6): p. 1391-1403.
- 673 [36] Wang, Z.M., et al., Determining individual mineral contributions to U(VI) adsorption in a  
674 contaminated aquifer sediment: A fluorescence spectroscopy study. *Geochimica Et*  
675 *Cosmochimica Acta*, 2011. 75(10): p. 2965-2979.
- 676 [37] Othmane, G., Allard, T., Vercoeur, T., Morin, G., Fayek, M., and Calas, G., Luminescence  
677 of uranium-bearing opals: Origin and use as a pH record. *Chemical Geology*, 2016. 423:  
678 pp. 1-6.
- 679 [38] Mei, H., et al., Uranium (VI) sorption on illite under varying carbonate concentrations:  
680 Batch experiments, modeling, and cryogenic time-resolved laser fluorescence  
681 spectroscopy study. *Applied Geochemistry*, 2022. 136: p. 105178.
- 682 [39] Baumann, D., et al., Detection of U(VI) on the surface of altered depleted uranium by  
683 time-resolved laser-induced fluorescence spectroscopy (TRLFS). *Science of the Total*  
684 *Environment*, 2006. 366: p. 905-909.
- 685 [40] Ramanujam, N., et al., Cervical precancer detection using a multivariate statistical  
686 algorithm based on laser-induced fluorescence spectra at multiple excitation  
687 wavelengths. *Photochemistry and Photobiology*, 1996. 64(4): p. 720-735
- 688 [41] Lewitzka, F, et al., Quantitative analysis of aromatic molecules in water by laser induced  
689 fluorescence spectroscopy and multivariate calibration techniques. *Proceedings of SPIE*,  
690 1999. 3821: p. 331-338.
- 691 [42] Amuah, C. L. Y., et al., Laser-induced fluorescence combined with multivariate  
692 techniques identifies the geographical origin of antimalarial herbal plants. *Journal of the*  
693 *Optical Society of America A*, 2020. 37(11): p. C103-C110.
- 694 [43] Drobot, B., et al., Speciation studies of metals in trace concentrations: the mononuclear  
695 uranyl(VI) hydroxo complexes. *Analytical Chemistry*, 2016. 88: p. 3548-3555.
- 696 [44] Belova, L.N., Formation conditions of oxidation zones of uranium deposits and uranium  
697 mineral accumulations in the gipergeneses zone. *Geology of Ore Deposits*, 2000. 42(2):  
698 p. 103-110.
- 699 [45] Savitzky, A., & Golay, M. J. E., Smoothing and differentiation of data by simplified least  
700 squares procedures. *Analytical Chemistry*, 1964(36): p. 1627-1639.
- 701 [46] Bian, X., *Spectral Preprocessing Methods*. In: *Chemometric Methods in Analytical*  
702 *Spectroscopy Technology*. Springer, Singapore, 2022.
- 703 [47] Lasch, P., et al., Imaging of colorectal adenocarcinoma using FT-IR microspectroscopy  
704 and cluster analysis. *Biochimica Biophysica Acta*, 2004. 1688(2): p. 176-186.
- 705 [48] Cebi, N., et al., A rapid ATR-FTIR spectroscopic method for detection of sibutramine  
706 adulteration in tea and coffee based on hierarchical cluster and principal component  
707 analyses. *Food Chemistry*, 2017. 229 : p. 517-526.

- 708 [49] Le Moyec, L., et al., Serum  $^1\text{H}$ -nuclear magnetic spectroscopy followed by principal  
709 component analysis and hierarchical cluster analysis to demonstrate effects of statins  
710 on hyperlipidemic patients. *NMR in Biomedicine*, 2005. 18(7) : p. 421-429.
- 711 [50] Long, W. J., et al., Fast identification of the geographical origin of *Gastrodia elata* using  
712 excitation-emission matrix fluorescence and chemometric methods. *Spectrochimica*  
713 *Acta B*, 2021. 258: 119798.
- 714 [51] Amuah, C. L. Y., et al., Laser-induced fluorescence combined with multivariate  
715 techniques identifies the geographical origin of antimalarial herbal plants. *J. Opt. Soc.*  
716 *Am. A*, 2020. 37(11): p. C103-C110.
- 717 [52] Dankowska, A., et al., Comparison of different classification methods for analyzing  
718 fluorescence spectra to characterize type and freshness of olive oils. *Eur. Food Res.*  
719 *Technol.*, 2019. 245(3): p. 745-752.
- 720 [53] Krivovichev, S.V. and J. Plasil, Mineralogy and Crystallography of uranium, in: *Uranium:*  
721 *from Cradle to Grave*. Eds: P.C. Burns and G.E. Sigmon. Mineralogical Association of  
722 Canada, Short Course Series, 2013. 43: p. 15-119.
- 723 [54] Oher, H., et al., Influence of Alkaline Earth Metal Ions on Structures and Luminescent  
724 Properties of  $\text{Na}_m\text{M}_n\text{UO}_2(\text{CO}_3)_3^{(4-m-2n)-}$  (M = Mg, Ca; m, n = 0–2): Time-Resolved  
725 Fluorescence Spectroscopy and Ab Initio Studies. *Inorg. Chem.*, 2020. 59(20): p. 15036-  
726 15049.
- 727 [55] Huber, F., Lützenkirchen, J., Uranyl retention on quartz: new experimental data and  
728 blind prediction using an existing surface complexation model. *Aquat. Geochem.*, 2009.  
729 15(3): pp. 443–456.
- 730 [56] Gabriel, U., Charlet, L., Schlapfer, C.W., Vial, J.C., Brachmann, A., and Geipel, G., Uranyl  
731 surface speciation on silica particles studied by time-resolved laser-induced  
732 fluorescence spectroscopy. *Journal of Colloid and Interface Science*, 2001. 239: pp. 358-  
733 368.
- 734 [57] Burns, P.C., The structure of boltwoodite and implications of solid solution toward  
735 sodium boltwoodite. *Canadian Mineralogist*, 1998. 36: p. 1069-1075.
- 736 [58] Plášil, J., Mineralogy, Crystallography and Structural Complexity of Natural Uranyl  
737 Silicates. *Minerals*, 2018. 8(12): p. 551.
- 738 [59] Burns, P.C., M.L. Miller, and R.C. Ewing,  $\text{U}^{6+}$  minerals and inorganic phases: A comparison  
739 and hierarchy of crystal structures. *Canadian Mineralogist*, 1996. 34: p. 845-880.
- 740 [60] Burns, P.C., R.C. Ewing, and F.C. Hawthorne, The crystal chemistry of hexavalent  
741 uranium: Polyhedron geometries, bond-valence parameters, and polymerization of  
742 polyhedra. *Canadian Mineralogist*, 1997. 35: p. 1551-1570.
- 743 [61] Kremleva, A., et al., Uranyl adsorption on solvated clay mineral surfaces. *Abstracts of*  
744 *Papers of the American Chemical Society*, 2010. 239.
- 745 [62] Burns, P.C.,  $\text{U}^{6+}$  minerals and inorganic compounds: Insights into an expanded structural  
746 hierarchy of crystal structures. *Canadian Mineralogist*, 2005. 43: p. 1839-1894.

747 [63] Tarafder, P. K., et al., Field method for the rapid determination of traces of uranium in  
748 rocks, soil and stream sediments by fluorescence measurement. J. Radioanal. Nucl.  
749 Chem., 2015. 306: p. 357-363.

Accepted preprint